Constructing pathway of mixed ion and electron transfer reactions for O_2 incorporation in $Pr_{0.1}Ce_{0.9}O_{2-x}$

Di Chen,[1,a] Zixuan Guan,[2] Dawei Zhang,[1] Lena Trotochaud,[3,b] Ethan Crumlin,[4] Slavomir Nemsak,[3] Hendrik Bluhm,[3,c] Harry L. Tuller,[5] and William C. Chueh [1,*]

[1] *Department of Materials Science & Engineering, Stanford University, Stanford, CA 94305, USA.*

[2] *Department of Applied Physics, Stanford University, Stanford, CA 94305, USA.*

[3] *Chemical Sciences Division, Lawrence Berkeley National Laboratory, Berkeley, CA 94720, USA.*

[4] *Advanced Light Source, Lawrence Berkeley National Laboratory, Berkeley, CA 94720, USA.*

[5] *Department of Materials Science and Engineering, Massachusetts Institute of Technology, Cambridge, MA 02139, USA.*

[a] *Present Address: The Future Laboratory, Tsinghua University, Beijing 100084, China.*

[b] *Present Address: Center for WaSH-AID, Duke University, Durham, NC 27701, USA.*

[c] *Present Address: Fritz Haber Institute of the Max Planck Society, 14195 Berlin, Germany.*

[*] *Correspondence and requests for materials should be addressed to W.C.C. (email: wchueh@stanford.edu).*

Abstract

In interfacial charge-transfer reactions, the complexity of the reaction pathway increases with the number of charges transferred, and becomes even greater when the reaction involves both electrons (charge) and ions (mass). These so-called mixed ion electron transfer (MIET) reactions are crucial in intercalation/insertion electrochemistry, such as those occurring in oxygen reduction/evolution electrocatalysts and lithium-ion battery electrodes. Understanding MIET reaction pathways, particularly identifying the rate-determining step (RDS), is crucial for engineering interfaces at the molecular, electronic, and point defect levels. Here we develop a generalizable experimental and analysis framework for constructing the O_2(g) incorporation reaction pathway in $Pr_{0.1}Ce_{0.9}O_{2-x}$. We converge on four candidate RDS (dissociation of neutral oxygen adsorbate) out of more than 100 possibilities by measuring the current density-overpotential curves while controlling both oxygen activity in the solid and the oxygen gas partial pressure, and quantifying the chemical and electrostatic driving forces using operando ambient pressure X-ray photoelectron spectroscopy.

Mixed ion and electron transfer (MIET) reactions involve the transfer of both ionic and electronic charges across interfaces. They are substantially more complex than electron transfer and proton-coupled electron transfer reactions because the ionic charge also crosses the electrochemical double layer.[1] The net reactions are usually chemical in nature (i.e., no net charge transfer). Examples include H^+ intercalation in layered hydroxides and Li^+ insertion in metal oxides (**Fig. 1a,b**).[2] Another ubiquitous example is the oxygen incorporation reaction (OIR) occurring at the solid/gas interface (**Fig. 1c**). It is rate-determining for many energy- and environment-related technologies, including oxygen storage materials for emission control,[3] solid oxide fuel cells (SOFCs),[4] electrolysis cells,[5] thermochemical water splitting cycles,[6] and oxygen permeation membranes.[7] The OIR is expressed as

$$O_2 + 4e^- \rightarrow 2O^{2-}. \quad (1)$$

Understanding the OIR reaction pathway is crucial for engineering and discovering catalysts, typically oxides, with high activity and stability.[8,9] Mixed ionic–electronic conductors (MIECs) have received widespread interests because they expand the effective OIR site to the gas/solid double-phase boundary beyond the traditional triple phase boundary between gas, ionic and electronic conductors.[10,11] There, oxygen ions and electrons react with oxygen adsorbates at the same active site, resulting in a reaction that involves the transfer of two oxygen ions and four electrons.

The number of charges transferred during OIR has made it challenging to isolate the rate-determining step (RDS). Most experimental work has focused on measuring the exchange coefficients[12] using tracer diffusion,[13] conductivity and mass relaxation,[14] and impedance spectroscopy,[15] as well as their reaction order with respect to oxygen gas pressure (pO_2) and activation energy.[16,17] The reaction order is then used to refine microkinetic models, typically by

assuming the nature of the reaction intermediates,[9,18–21] sometimes with the assistance of atomistic simulations.[21,22] While useful, these methods convolute forward and reverse reaction rate constants and do not consider crucial information about the RDS encoded in the overpotential dependence of the current density (i.e., the Tafel slope). In studies in which the current density–overpotential (j-η) curves are measured, analysis of the Tafel slope is non-trivial because the slope is a natural convolution of electrostatic driving forces (surface potential) and chemical driving forces (oxygen activity in the solid state, $a\mathrm{O_2}$). Similarly, analysis of the $\mathrm{O_{2(g)}}$ reaction order is also non-trivial because $p\mathrm{O_2}$ affects not only oxygen gas but also the concentration of solid-state point defects at the gas/MIEC(oxide) interface,[23,24] of which the procedures for measurement have been developed recently.[25,26] Finally, the availability of ionic and electronic species for OIR are generally inferred from the bulk measurements, whereas recent studies have shown that the surface chemistry and stoichiometry can differ significantly from those of the bulk. Moreover, the surface can also deviate from electroneutrality.[27–29]

To isolate the RDS of OIR, one must address the challenging task of experimentally determining the surface point defect chemistry, quantifying the electrostatic and chemical driving forces, and interpreting the $\mathrm{O_{2(g)}}$ reaction order and the Tafel slope simultaneously. In this work, we present an experimental and analysis framework and apply it to OIR on $\mathrm{Pr_{0.1}Ce_{0.9}O_{2-x}}$ (praseodymium-cerium oxide, PCO), a promising SOFC cathode with a well-established point defect chemistry.[30–32] Combining current density–overpotential with *operando* surface potential and electron concentration measurements, we probe the roles of oxygen vacancies and electrons in the four-electron/two-ion MIET reaction and converge on the RDS: the dissociation of neutral molecular oxygen adsorbate. This generalizable method can also be applied to study other MIET reactions, including those occurring at solid–liquid and solid–solid interfaces.

Results

Microkinetic model

Before discussing the microkinetic framework for analyzing OIR reaction order and Tafel slope, we briefly review the equilibrium point defect chemistry of PCO.[30,33] The charge carriers are small polaronic electrons and oxygen vacancies generated via the reduction of Pr^{4+} to Pr^{3+} with decreasing aO_2, as described by the following reaction written in Kröger–Vink notation:

$$O_2(g) + 4Pr'_{Ce} + 2V_O^{\bullet\bullet} \leftrightarrow 4Pr_{Ce}^{\times} + 2O_O^{\times} \quad (2)$$

where electrons (or equivalently Pr^{3+}) are denoted by Pr'_{Ce}, oxygen vacancies by $V_O^{\bullet\bullet}$, and Pr^{4+} by $Pr_{Ce}^{\times}$. The Ce^{4+}/Ce^{3+} redox pair does not participate in OIR under oxidizing conditions.[30,33] Bulk defect activities are shown in Supplementary Note 1.

In our microkinetic model,[25] we assume that one elementary reaction step is the RDS and that all the other elementary steps occur in series and are in quasi-equilibrium. We group the elementary steps into preceding, rate-determining, and following steps.[1] Rather than explicitly specifying these intermediate species as done in previous work,[17,18,34,35] we use $\{O^*\}$ and $\{O^{**}\}$ to denote the reactant(s) and product(s) of the oxygen intermediate(s) involved in the RDS, respectively. The reaction pathway is written generally as follows:

Preceding reaction:

$$O_2 + \nu_{V,1} V_O^{\bullet\bullet} + \nu_{e,1} Pr'_{Ce} \rightarrow n\{O^*\} + \nu_{e,1} Pr_{Ce}^{\times} \quad (3)$$

RDS:

$$n \times \left(\{O^*\} + \nu_{V,2} V_O^{\bullet\bullet} + \nu_{e,2} Pr'_{Ce} \rightarrow \{O^{**}\} + \nu_{e,2} Pr_{Ce}^{\times} \right) \quad (4)$$

Following reaction:

$$n\times\left(\{O^{**}\}+\nu_{V,3}V_O^{\bullet\bullet}+\nu_{e,3}Pr_{Ce}^{\prime}\rightarrow 2/nO_O^{\times}+\nu_{e,3}Pr_{Ce}^{\times}\right) \quad (5)$$

Here $\nu_{V,1}$, $\nu_{V,2}$ and $\nu_{V,3}$ are stoichiometric coefficients corresponding to the number of oxygen vacancies participating in the preceding, rate-determining, and following steps. Analogously, $\nu_{e,1}$, $\nu_{e,2}$, and $\nu_{e,3}$ are the stoichiometric coefficients of the electrons in these steps (the possible roles of electron-holes will be discussed later). Thus, these integer stoichiometric coefficients sum up to 2 and 4, respectively. The RDS can occur more than once. For example, if one O_2 molecule dissociates into two identical atomic oxygen adsorbates preceding the RDS, then the RDS will occur twice. We use n to specify the number of times that the RDS repeats per O_2 gas molecule.

Under strongly cathodic conditions, the anodic current density is negligible, and the current density can be written as (detailed in Supplementary Note 3):

$$j\propto pO_2^{1/n}aO_2^{\lambda}\exp\left(\frac{\left(\beta z-\gamma_{\mathrm{pre}}/n\right)e\chi}{k_BT}\right), \quad (6)$$

where

$$\lambda=\left(\frac{\nu_{V,1}}{n}+\nu_{V,2}\right)\frac{\partial\log a\left(V_O^{\bullet\bullet}\right)}{\partial\log aO_2}\bigg|_{T,pO_2}+\left(\frac{\nu_{e,1}}{n}+\nu_{e,2}\right)\frac{\partial\log a\left(Pr_{Ce}^{\prime}\right)}{\partial\log aO_2}\bigg|_{T,pO_2}-\frac{\nu_{e,1}}{n}\frac{\partial\log a\left(Pr_{Ce}^{\times}\right)}{\partial\log aO_2}\bigg|_{T,pO_2} \quad (7)$$

$$aO_2=pO_2\exp\left(\frac{4e\eta}{k_BT}\right). \quad (8)$$

Eq. 8, which is the Nernst equation, describes the relationship between the oxygen partial pressure in the gas phase and the oxygen activity in the electrode. There are two degrees of freedom between overpotential (η), pO_2 and aO_2. For clarity, constants and equilibrium concentrations and potential are not shown in Eq. 6. Here, z is the total number of electrons

123 and/or ions migrating across the gas–solid interface in the RDS; β is the symmetry parameter of
124 this electrochemical step (if $z \neq 0$); and γ_{pre} determines the dependence of the preceding
125 equilibrium on the surface potential χ .

126 The kinetic parameters n and λ in Eq. 6 reflect the reaction mechanism: n , as
127 mentioned, represents the number of times that the RDS repeats and directly describes the
128 dependence of the current density on $p\mathrm{O}_2$; λ is a measure of the overall dependence of point
129 defect activities on $a\mathrm{O}_2$. We point out that, for a given combination of $a\mathrm{O}_2$, $p\mathrm{O}_2$ and
130 overpotential, the electrode and the surface chemistry can be unique. Therefore, n can depend on
131 $a\mathrm{O}_2$, and likewise lambda can depend on $p\mathrm{O}_2$. The model reconciles adsorbate chemistry with
132 point defect chemistry at the solid/gas interface under electrochemical bias. Next, we
133 experimentally obtain n and λ , and shed light on the kinetics of MIET steps in OIR.
134

135 **Electrochemical characteristics**

136 We fabricated 150 nm-thick dense thin film PCO electrodes on single crystalline yttria-
137 stabilized zirconia (YSZ) solid electrolytes via pulsed-laser deposition (see Methods section for
138 details). A buried Pt microfabricated current collector is used to eliminate its contribution to the
139 reaction pathway and to ensure uniform electronic current collection. An oversized and highly
140 active counter electrode was also used to eliminate contributions from the counter electrode. In
141 this cell configuration, electrochemical polarization at the Pt/YSZ interface drives the chemical
142 OIR at the gas/solid interface. We note that electronic conductivity in PCO decreases with $p\mathrm{O}_2$:
143 above ~ 10^{-3} atm, impedance spectroscopy indicates an in-plane electronic transport gradient.
144 This is a result of the geometry of microfabricated current collector employed. For this reason,
145 we limit the $p\mathrm{O}_2$ to below ~ 10^{-3} atm, which is lower than that in typical SOFC cathodes.

Current density–overpotential curves were measured as functions pO_2 at 600°C, both using a conventional electrochemical rig and a button heater inside an ambient pressure X-ray photoelectron spectroscopy (APXPS) chamber**.** The overpotential-dependent current density at different pO_2 values at 600°C is shown in **Fig. 2a**. We then calculated aO_2 via the Nernst equation (Eq. 8), and plot the current density as a function of both aO_2 and pO_2 (**Fig. 2b**).[26] We verified that the electrode had reached steady state and that degradation is not convoluting the measurement (Supplementary Fig. 1a). Reproducibility was excellent among four cells (**Fig. 2c**). We note that the area-specific resistance at open-circuit are approximately two-orders-of-magnitude lower than those reported in a previous study,[36] though the reaction order with pO_2 is comparable. We attribute this improvement to the lower impurity level in this study; only Au & Pt wires and alumina were in contact with the sample and the hot gas in contrast to previous measurements[37]. The reaction order measured in this study also agrees broadly with Simons et al., in which a reaction order of 0.67 was measured by a mass relaxation method on PCO.[38] We also carried out impedance spectroscopy under bias (Supplementary Fig. 1b). The Nyquist plot is well described by a simple serial resistor-capacitor network. For Ohmic-corrected overpotentials from -200 mV to 0 mV, the absence of a Warburg-like feature confirms that electronic and ionic diffusion gradients are small, even under bias, indicating that our cell is limited by the OIR surface reaction. Nevertheless, we cannot completely rule out equilibrium or transport gradients in the near-surface region. If such a gradient exists, one has to relate the oxygen activity at the surface to that in the bulk.

The application of Eq. 8 requires precise measurement and control of overpotential, which is challenging for solid-state electrochemical cells.[39,40] To confirm that we indeed have measured the overpotential accurately, we use the chemical capacitance (C_{chem}) of PCO as an internal

gauge of aO_2 (**Fig. 2d**). We find that C_{chem} is only a function of aO_2 at open circuit and under bias*, i.e.,* values measured at different aO_2 (either by changing pO_2 or changing the overpotential) collapses on a single line. This directly confirms that overpotential was accurately determined. Fitting a bulk defect chemical model to C_{chem} in our thin-film electrode gives defect formation energetics comparable to bulk values (Supplementary Note 2).

Operando characterization of gas/solid interface

As localized electrons on the PCO surface are reactants of OIR, we used operando Pr M-edge X-ray absorption spectroscopy (XAS) in partial electron-yield detection mode to determine the near surface oxidation state of PCO as a function of overpotential (**Fig. 3a,b**). Two end members (spectra measured at +400 mV/ 450°C and spectra measured at -400 mV/ 600°C) are consistent with Pr^{4+} and Pr^{3+} states, respectively[41,42] (Supplementary Fig. 6). We then obtained the fraction of Pr in the 3+ state, [Pr^{3+}], through a linear combination fitting consisting of the end members (**Fig. 3b,c**, Supplementary Fig. 7). The results are comparable to that reported by Lu *et al.* at 450°C.[43] Fig. 3c compares the surface defect concentrations to bulk values. Pr becomes fully reduced to 3+ at comparable aO_2, both at the surface and in the bulk; at more oxidizing aO_2; the surface is slightly more reduced than the bulk. Direct quantification of surface oxygen vacancies, the other important participant in OIR, was not possible, likely reflecting a low concentration due to PCO having a bulk oxygen vacancy concentration of ≤ 2.5% (Supplementary Fig. 4c).

The presence of charged adsorbates and charged ions near the surface establishes a potential drop, χ; deviation relative to open-circuit value contributes the reaction rate.[23,25,44] For a metal electrode, such potential drop is trivially related to the overpotential. However, for a MIEC, it

cannot be inferred from electrochemical measurement nor independently controlled. Here, we estimate χ using operando APXPS via shifts of O 1s photoemission peaks.[45–47] Measurements were performed at oxygen gas pressures ranging from 0.03 to 1 Torr O_2 atmosphere at 600 °C. Specifically, we compare the binding energy (BE) of oxygen gas and lattice oxygen on the PCO surface (**Fig. 3d**), which was carried out at the same time as the XAS measurement. For the lattice oxygen peak, we identified a total of three oxygen species at an information depth of ~0.6 nm (for the definition of surface sensitivity, see Ref. [45]). Based on earlier photoemission studies, we assigned the most intense peak (the blue peak denoted as O) to bulk-like lattice oxygen in PCO.[45] The two smaller peaks at relative BEs of ~1.2 and ~2.6 eV (the purple peak denoted as O' and cyan peak denoted as O'', respectively) are attributed to oxygen bonded to segregated silicon impurities and surface adsorbates. These relative BEs between O', O'', and lattice O did not change with bias or pO_2 (Supplementary Fig. 4b).

We now consider the BEs of the oxygen-gas and lattice oxygen, the difference of which is related to the surface potential.[45] As shown in Fig. 3d, the spectra of the oxygen-gas and oxygen-lattice core levels both shift systematically with applied overpotential. Quantitative analysis reveals that both the oxygen-gas and oxygen-lattice core levels both shifted by approximately 1 eV per 1 V overpotential applied (Supplementary Fig. 4a). This means that the surface potential is essentially constant under all conditions examined (**Fig. 3e**), simplifying the current density expression in Eq. 6 to $j \propto pO_2^{1/n} aO_2^{\lambda}$. This result is consistent with the findings of our recent study of CeO_{2-x}, in which only strongly polar adsorbates (such as OH^-) induce a change in χ with overpotential.[45]

Analysis of current density–overpotential curves

To obtain the $O_{2(g)}$ reaction order ($1/n$), the slope of log$j$-logpO_2 was evaluated at constant aO_2 values (**Fig. 4a**); n has an average of ~ 1.3 from measurement of three electrodes and is largely independent of aO_2, indicating that the RDS occurs once (**Fig. 4c**). This directly suggests that the RDS involves a molecular oxygen intermediate. The deviation from 1 may be explained by non-dilute adsorption surface sites（details in Supplementary Note 9）and/or the emergence of co-limiting RDS steps.[48] We followed a similar procedure to obtain λ, the reaction order on aO_2 (**Fig. 4b, d**). We obtain an average value for λ of -0.13, which tends to 0 at low aO_2.

At first glance, given λ, it appears to be straightforward to use Eq. 7 to solve the combination of stoichiometric coefficients ($\nu_{V,i}$ and $\nu_{e,i}$) in Eq. 3–5 to identify the MIET pathway. These coefficients enable the number of electrons and oxygen vacancies before, during, and after the RDS to be determined. However, we are missing one crucial parameter. As shown in Eq. 7, interpreting λ requires knowing the oxygen vacancy concentration at the PCO surface, which could not be determined experimentally due to its dilute concentration. While it is common to invoke electroneutrality approximation to estimate this quantity, the surface may not be electroneutral.[27–29]

Here, we developed a procedure to estimate these stoichiometric coefficients without knowing the oxygen vacancy concentration. In total, we consider 108 combinations of integer values of n, $\nu_{V,i}$, and $\nu_{e,i}$ (Supplementary Table 2). Each combination corresponds to a possible MIET pathway. Knowing that the OIR proceeds via a molecular pathway, we excluded all the combinations containing n=2, leaving 90 possible pathways. Next, we simulate how λ varies with pO_2 for these pathways and compare them to the experimentally measured values. For

$\frac{\partial \log[\mathrm{Pr}'_{\mathrm{Ce}}]}{\partial \log aO_2}$, we used the surface values measured by *operando* XAS (since $[\mathrm{Pr}'_{\mathrm{Ce}}] \ll 1$). To address the issue of not knowing the surface oxygen vacancy concentration, we specifically investigate three limiting scenarios. First, we consider $2[V_O^{\cdot\cdot}] = [Pr^{3+}]$, which corresponds to an electroneutral surface. Second, we consider $\frac{\partial \log[V_O^{\cdot\cdot}]}{\partial \log aO_2} = 0$, whereby oxygen vacancies is decoupled from electrons leading to build up of charge, and the surface is saturated with oxygen vacancies such that they do not change with oxygen partial pressure. Finally, we consider $\frac{\partial \log[V_O^{\cdot\cdot}]}{\partial \log aO_2} = -1$, which represents a scenario in which oxygen vacancy concentration decreases with oxygen partial pressure more sharply than in the electroneutral case; defect-defect interactions and other non-idealities could lead to this situation. The simulated defect concentrations under those scenarios are plotted in **Fig. 5a**, and the corresponding λ values for the 90 candidate molecular pathways are shown in **Fig. 5b.** Experimentally, we observed that λ tends to 0 under reducing conditions (low aO_2). For all three oxygen vacancy limits considered, only $\nu_{e,1} = 0$ (no electrons transferred before RDS) yields this behavior (Fig. 5b); Indeed, satisfactory fits to lambda can be obtained only for $\nu_{e,1}=0$, while other values of $\nu_{e,1}$ (1 to 4) yield λ which are inconsistent with the experimentally measured values. This is because the third term in Eq. 7 scales directly with $\nu_{e,1}$. With this insight, the number of possible pathways then decreases considerably from 90 to 30.

To further converge on the reaction pathway, we take the experimental value of λ, and back calculate $\frac{\partial \log[V_O^{\cdot\cdot}]}{\partial \log aO_2}$ for the 30 remaining combinations of stoichiometric numbers of electrons

and oxygen vacancies (**Fig. 5c).** We exclude all the combinations that give a positive $\frac{\partial \log[V_O^{\cdot\cdot}]}{\partial \log aO_2}$ value because the surface oxygen vacancy concentration is unlikely to increase with aO_2. This constraint further lowers the possible combinations from 30 to 6; these six combinations are tabulated in **Fig. 6** along with their corresponding RDS. Notably, $\nu_{e,1}$ (number of electrons transferred before RDS) and $\nu_{e,2}$ (number of electrons transferred during RDS) are zero for all the combinations in Fig. 6. In other words, electrons are not involved before or during the RDS. In fact, these six reaction pathways are the only ones with this feature among the original 108 combinations.

Now, we take a closer look at these remaining six possibilities. Reaction pathway A can be easily excluded, as it results in a zero O_2 reaction order ($\lambda = 0$) for all pO_2, which is inconsistent with experiments in Fig. 4d. This result is natural as the RDS in reaction A corresponds to O_2(g) adsorption, which leads to a current density that is independent of the defect concentration in the bulk (hence $\lambda = 0$). Reaction pathway F is also unlikely, as it means that the O_2(g) molecule has been incorporated into a cluster containing two adjacent oxygen vacancies prior to the RDS (because two oxygen vacancies were transferred before the RDS while the oxygen intermediate remaining molecular). The remaining four reaction pathways, B-E, share two common features: (1) the RDS involves a molecular oxygen adsorbate, and (2) electrons are not transferred before or during the RDS. In other words, the RDS is an O_2 dissociation process that involves neutral O_2 (without having been reduced). The difference among the four pathways concerns whether 0, 1 or 2 oxygen vacancies are involved in the RDS. For pathways B and C, the initial state involves molecular oxygen adsorbates, whereas for pathways D and E, the initial state involves molecular oxygen already incorporated into an oxygen vacancy. We can also differentiate the

277 pathways based on the final state. In pathways B and D, the final state is one incorporated
278 oxygen ion and one atomic oxygen adsorbate; in pathway C and E, the final state is two
279 incorporate oxygen ions. Our conclusion is consistent with a recent study by Schaube et al. The
280 authors investigated the RDS of PCO using a pulsed isotope exchange method, and found
281 molecular oxygen species are involved in the RDS (in addition to oxygen vacancies).[49]

282 We note that in MIECs such as $SrTi_{1-x}Fe_xO_{3-\delta}$, it has been proposed that minority electronic
283 species, rather than majority, participates in RDS.[34] For completeness, we simulated λ assuming
284 holes (presumably oxygen holes) are involved in the RDS. The reaction order is not sensitive to
285 whether no electrons or some holes are involved (Supplementary Note 10). Our analysis
286 indicates that studies under anodic overpotentials are needed, which are being pursued.
287 Nevertheless, this ambiguity does not affect the conclusion that the RDS is likely the dissociation
288 of a neutral O_2 adsorbate.

289 This insight into the reaction mechanism can be used to improve the catalytic activity of ceria
290 as well as other materials for OIR. Because electrons are not involved before or during the RDS,
291 lowering the electron transfer barrier or increasing concentrations are not expected to
292 significantly improve the surface catalytic activity. Instead, efforts should be focused on
293 decreasing barrier height for O_2 dissociation and for oxygen incorporation into vacancies and
294 increasing concentrations.[50] This insight may also apply to other oxygen-incorporation catalysts
295 that are limited by the availability of surface oxygen vacancies.

296 In summary, we developed a generalizable experimental and analysis framework to identify
297 the RDS for the oxygen incorporation reaction on $Pr_{0.1}Ce_{0.9}O_{2-x}$, a promising cathode for solid-
298 oxide fuel cells. By simultaneously measuring how current density depends on oxygen partial
299 pressure and overpotential, as well as how the surface electron concentration and electrostatic

potential vary, we eliminate a vast majority of the candidate MIET reaction pathways. The rich information encoded in the oxygen partial pressure and overpotential dependences makes it possible to converge on four possible reaction pathways, even though surface oxygen vacancy concentration could not be measured directly. The robust conclusion that the RDS is likely the dissociation of neutral molecular oxygen adsorbate provides important mechanistic insight that could further guide the optimization of oxygen incorporation (electro)catalysts. This analysis method can be straightforwardly extended to other oxygen-ion-conducting electrodes, as well as to other chemistries to unravel the microkinetics of MIET reactions.

Methods

Sample preparation: Thin-film electrochemical cells were fabricated on 10 × 10 × 0.5 mm (100) $Y_{0.16}Zr_{0.84}O_{1.92}$ (YSZ) single-crystal substrates (MTI Corp.) that served as the oxygen-ion-conducting solid electrolyte. The fabrication procedure is described below in chronological order. First, a Pt patterned current collector (5 μm line width and 30 μm) was fabricated on the smooth side of the substrate using metal lift-off photolithography. The fabrication procedure was reported previously.[51] Then, 200-nm-thick LSCF ($La_{0.6}Sr_{0.4}Co_{0.2}Fe_{0.8}O_{3-\delta}$) thin films were deposited on the back of the YSZ as the counter electrode using pulsed-laser deposition (PLD). A 20-nm-thick $Sm_{0.2}Ce_{0.8}O_{1.9}$ (SDC) buffer layer was also deposited to suppress cation interdiffusion between the YSZ and LSCF thin film. The PLD deposition was performed at 700°C and 5 mTorr O_2 with a laser fluence of 1.5 J/cm^2 at 10 Hz and a substrate-to-target distance of 70 mm. The high activity and large area of the counter electrode guaranteed that the counter-electrode reaction did not limit the cell performance. Finally, 150-nm-thick $Pr_{0.1}Ce_{0.9}O_2$

(PCO) thin films were deposited using PLD. An Inconel shadow masks, with an opening of 0.5 × 2 mm, was employed to deposit PCO on top of the Pt-patterned current collector. The PLD deposition was performed at 700°C and 5 mTorr O_2 with a laser fluence of 1.5 J/cm^2 at 10 Hz and a substrate-to-target distance of 70 mm.

A solid-state method was used to prepare PCO polycrystalline targets. Pr_6O_{11} and CeO_2 high-purity powders (99.99%, Sigma-Aldrich) were weighed according to the desired stoichiometry, ground in a mortar, and then pressed into 1-inch-radius pellets. The as-obtained pellets were calcined at 900°C for 5 h and then at 1250°C for 9 h in Ar to obtain dense targets for PLD. A similar procedure was used to fabricate the LSCF target, the details of which were previously reported.[52]

Sample characterization: X-ray diffraction patterns of the as-deposited thin films were obtained in the 2θ range of 20°–80° (PANalytical X'Pert PRO, Cu Kα radiation). The films crystallized in the cubic fluorite structure (Supplementary Fig. 3). The film thickness was determined using a surface profilometer (Dektak 150, Veeco). The thin film composition was examined using inductively coupled plasma mass spectrometry (ICP-MS, Thermo Scientific XSERIES 2). The surface morphology was characterized using atomic force microscopy (Park Systems XE-100).

Electrochemical measurements: Electrochemical measurements were performed using a custom electrochemical testing system that did not use any metal paste or silicon-containing materials. The aim was to use high-purity alumina and noble metals to reduce or eliminate the convoluting effects of binding agents in metal pastes, as these agents can combust or volatize. A gas manifold of synthetic high-purity gas mixtures of O_2 balanced with Ar was used to control

the oxygen partial pressure, pO_2, using MKS P4B mass-flow controllers.

Electrochemical ambient pressure X-ray photoelectron spectroscopy: The measurement was carried out at beamlines 11.0.2 and 9.3.2 of the Advanced Light Source at Lawrence Berkeley National Laboratory.[53] The samples were mounted onto a gold mesh (counter) on the ceramic heater of a custom-made heating and biasing stage.[54] Pt–Ir (10%–20% Ir) wires were used as an electrical contact and to hold the working electrode onto the heater. The temperature was determined from the ohmic offset of YSZ using electrochemical impedance spectroscopy (Biologic SP-300 potentiostat) of model dense Pt film devices calibrated in a tube furnace with a thermocouple near the device. The entire APXPS experiment was performed under defined bias, and the alternating voltage perturbation was 10 mV.

Electrochemical ambient pressure X-ray absorption spectroscopy: *Operando* XAS in partial-electron-yield detection mode was measured at 100 mTorr O_2 at 450°C and 600°C at beamline 11.0.2 of the Advanced Light Source at Lawrence Berkeley National Laboratory.[53] The sample mounting, temperature calibration, and electrochemical measurements were the same as those used for the APXPS experiment. The background was removed from the spectra by fitting a line to the Pr M_4 pre-edge. The spectra were subsequently normalized by the Pr M_5 post-edge.

Data availability: Source data that support the findings of this study are available from the corresponding author upon request.

References

1. Bard, A. J. & Faulkner, L. R. *Electrochemical Methods: Fundamentals and Applications, 2nd Edition*. (Wiley Textbooks, 2000).
2. Li, Y. & Chueh, W. C. Electrochemical and chemical insertion for energy transformation and switching. *Annu. Rev. Mater. Res.* **48**, 1–29 (2018).
3. Yao, H. C. & Yao, Y. F. Y. Ceria in automotive exhaust catalysts. I. Oxygen storage. *J. Catal.* **86**, 254–265 (1984).
4. Graves, C., Ebbesen, S. D., Jensen, S. H., Simonsen, S. B. & Mogensen, M. B. Eliminating degradation in solid oxide electrochemical cells by reversible operation. *Nat Mater* **14**, 239–244 (2015).
5. Irvine, J. T. S. *et al.* Evolution of the electrochemical interface in high-temperature fuel cells and electrolysers. *Nat. Energy* **1**, 15014 (2016).
6. Chueh, W. C. *et al.* High-flux solar-driven thermochemical dissociation of CO_2 and H_2O using nonstoichiometric ceria. *Science* **330**, 1797–1801 (2010).
7. Shao, Z. *et al.* Investigation of the permeation behavior and stability of a $Ba_{0.5}Sr_{0.5}Co_{0.8}Fe_{0.2}O_{3-\delta}$ oxygen membrane. *J. Memb. Sci.* **172**, 177–188 (2000).
8. Riva, M. *et al.* Influence of surface atomic structure demonstrated on oxygen incorporation mechanism at a model perovskite oxide. *Nat. Commun.* **9**, 3710 (2018).
9. Merkle, R. & Maier, J. How is oxygen incorporated into oxides? A comprehensive kinetic study of a simple solid-state reaction with $SrTiO_3$ as a model material. *Angew. Chem. Int. Ed. Engl.* **47**, 3874–94 (2008).
10. Adler, S. B. Factors governing oxygen reduction in solid oxide fuel cell cathodes. *Chem. Rev.* **104**, 4791–4843 (2004).
11. Chueh, W. C., Hao, Y., Jung, W. & Haile, S. M. High electrochemical activity of the oxide phase in model ceria-Pt and ceria-Ni composite anodes. *Nat. Mater.* **11**, 155–61 (2012).
12. Maier, J. On the correlation of macroscopic and microscopic rate constants in solid state chemistry. *Solid State Ionics* **112**, 197–228 (1998).
13. Kilner, J. A., De Souza, R. A. & Fullarton, I. C. Surface exchange of oxygen in mixed conducting perovskite oxides. *Solid State Ionics* **86**–**88**, 703–709 (1996).
14. Gopal, C. B. & Haile, S. M. An electrical conductivity relaxation study of oxygen transport in samarium doped ceria. *J. Mater. Chem. A* **2**, 2405–2417 (2014).
15. Baumann, F. S. *et al.* Quantitative comparison of mixed conducting SOFC cathode materials by means of thin film model electrodes. *J. Electrochem. Soc.* **154**, B931 (2007).
16. Fleig, J., Merkle, R. & Maier, J. The $p(O_2)$ dependence of oxygen surface coverage and exchange current density of mixed conducting oxide electrodes: model considerations. *Phys. Chem. Chem. Phys.* **9**, 2713 (2007).
17. Merkle, R. & Maier, J. Oxygen incorporation into Fe-doped $SrTiO_3$: Mechanistic interpretation of the surface reaction. *Phys. Chem. Chem. Phys.* **4**, 4140–4148 (2002).
18. De Souza, R. A. A universal empirical expression for the isotope surface exchange coefficients (k*) of acceptor-doped perovskite and fluorite oxides. *Phys. Chem. Chem. Phys.* **8**, 890–897 (2006).
19. Jung, W. & Tuller, H. L. Investigation of surface Sr segregation in model thin film solid oxide fuel cell perovskite electrodes. *Energy Environ. Sci.* **5**, 5370–5378 (2012).
20. Adler, S. B., Chen, X. Y. & Wilson, J. R. Mechanisms and rate laws for oxygen exchange on mixed-conducting oxide surfaces. *J. Catal.* **245**, 91–109 (2007).

21. Cao, Y., Gadre, M. J., Ngo, A. T., Adler, S. B. & Morgan, D. D. Factors controlling surface oxygen exchange in oxides. *Nat. Commun.* **10**, 1346 (2019).
22. Mastrikov, Y. A., Merkle, R., Heifets, E., Kotomin, E. A. & Maier, J. Pathways for oxygen incorporation in mixed conducting perovskites: A DFT-based Mechanistic analysis for (La, Sr)$MnO_{3-\delta}$. *J. Phys. Chem. C* **114**, 3017–3027 (2010).
23. Fleig, J. J. On the current–voltage characteristics of charge transfer reactions at mixed conducting electrodes on solid electrolytes. *Phys. Chem. Chem. Phys.* **7**, 2027–2037 (2005).
24. Tuller, H. L. & Bishop, S. R. Point defects in oxides: tailoring materials through defect engineering. *Annu. Rev. Mater. Res.* **41**, 369–398 (2011).
25. Guan, Z., Chen, D. & Chueh, W. C. Analyzing the dependence of oxygen incorporation current density on overpotential and oxygen partial pressure in mixed conducting oxide electrodes. *Phys. Chem. Chem. Phys.* **19**, 23414–23424 (2017).
26. Schmid, A., Rupp, G. M. & Fleig, J. Voltage and partial pressure dependent defect chemistry in (La,Sr)$FeO_{3-\delta}$ thin films investigated by chemical capacitance measurements. *Phys. Chem. Chem. Phys.* **20**, 12016–12026 (2018).
27. Zurhelle, A. F., Tong, X., Klein, A., Mebane, D. S. & De Souza, R. A. A space-charge treatment of the increased concentration of reactive species at the surface of a ceria solid solution. *Angew. Chemie - Int. Ed.* **56**, 14516–14520 (2017).
28. De Souza, R. A. The formation of equilibrium space-charge zones at grain boundaries in the perovskite oxide $SrTiO_3$. *Phys. Chem. Chem. Phys.* **11**, 9939–9969 (2009).
29. De Souza, R. A. & Martin, M. Using $^{18}O/^{16}O$ exchange to probe an equilibrium space-charge layer at the surface of a crystalline oxide: Method and application. *Phys. Chem. Chem. Phys.* **10**, 2356–2367 (2008).
30. Chen, D., Bishop, S. R. & Tuller, H. L. Non-stoichiometry in oxide thin films: a chemical capacitance study of the praseodymium-cerium oxide system. *Adv. Funct. Mater.* **23**, 2168–2174 (2013).
31. Chen, D., Bishop, S. R. S. & Tuller, H. L. Praseodymium-cerium oxide thin film cathodes: Study of oxygen reduction reaction kinetics. *J. Electroceramics* **28**, 62–69 (2012).
32. Seo, H. G., Choi, Y. & Jung, W. Exceptionally enhanced electrode activity of (Pr,Ce)$O_{2-\delta}$-based cathodes for thin-film solid oxide fuel cells. *Adv. Energy Mater.* **1703647**, 1–7 (2018).
33. Bishop, S. R., Stefanik, T. S. & Tuller, H. L. Electrical conductivity and defect equilibria of $Pr_{0.1}Ce_{0.9}O_{2-\delta}$. *Phys. Chem. Chem. Phys.* **13**, 10165–73 (2011).
34. Jung, W. & Tuller, H. L. A new model describing solid oxide fuel cell cathode kinetics: model thin film $SrTi_{1-x}Fe_xO_{3-\delta}$ mixed conducting oxides-a case study. *Adv. Energy Mater.* **1**, 1184 (2011).
35. Kuklja, M. M., Kotomin, E. a., Merkle, R., Mastrikov, Y. a. & Maier, J. Combined theoretical and experimental analysis of processes determining cathode performance in solid oxide fuel cells. *Physical Chemistry Chemical Physics* **15**, 5443–5471 (2013).
36. Chen, D. Characterization and Control of Non-stoichiometry in $Pr_{0.1}Ce_{0.9}O_{2-\delta}$ thin films: Correlation with SOFC Electrode Performance. (MASSACHUSETTS INSTITUTE OF TECHNOLOGY, 2014).
37. Zhao, L., Perry, N. H., Daio, T., Sasaki, K. & Bishop, S. R. Improving the Si impurity tolerance of $Pr_{0.1}Ce_{0.9}O_{2-\delta}$ SOFC electrodes with reactive surface additives. *Chem. Mater.* **27**, 3065–3070 (2015).

38. Simons, P., Ji, H. Il, Davenport, T. C. & Haile, S. M. A piezomicrobalance system for high-temperature mass relaxation characterization of metal oxides: A case study of Pr-doped ceria. *J. Am. Ceram. Soc.* **100**, 1161–1171 (2017).
39. Riess, I. Characterization of solid oxide fuel cells based on solid electrolytes or mixed ionic electronic conductors. *Solid State Ionics* **90**, 91–104 (2003).
40. Adler, S. B. Reference electrode placement in thin solid electrolytes. *J. Electrochem. Soc.* **149**, E166 (2002).
41. Thole, B. T. *et al.* 3d x-ray-absorption lines and the $3d^9 4f^{n+1}$ multiplets of the lanthanides. *Phys. Rev. B* **32**, 5107–5118 (1985).
42. Karnatak, R. *et al.* X-ray absorption studies of CeO_2, PrO_2, and TbO_2. I. Manifestation of localized and extended f states in the 3d absorption spectra. *Phys. Rev. B. Condens. Matter* **36**, 1745–1749 (1987).
43. Lu, Q. *et al.* Surface defect chemistry and electronic structure of $Pr_{0.1}Ce_{0.9}O_{2-\delta}$ revealed in operando. *Chem. Mater.* **30**, 2600–2606 (2018).
44. Chueh, W. C. & Haile, S. M. Electrochemistry of mixed oxygen ion and electron conducting electrodes in solid electrolyte cells. *Annu. Rev. Chem. Biomol. Eng.* **3**, 313–41 (2012).
45. Feng, Z. A. *et al.* Origin of overpotential-dependent surface dipole at CeO_{2-x}/gas interface during electrochemical oxygen insertion reactions. *Chem. Mater.* **28**, 6233–6242 (2016).
46. Nenning, A. *et al.* Ambient pressure XPS study of mixed conducting perovskite-type SOFC cathode and anode materials under well-defined electrochemical polarization. *J. Phys. Chem. C* **120**, 1461–1471 (2016).
47. Siegbahn, H. & Lundholm, M. A method of depressing gaseous-phase electron lines in liquid-phase ESCA spectra. *J. Electron Spectros. Relat. Phenomena* **28**, 135–138 (1982).
48. Guan, Z. Probing and Tuning Far-from-Equilibrium Oxygen Exchange Kinetics on Electrochemical Solid-Gas Interfaces. (Stanford University, 2018).
49. Schaube, M., Merkle, R. & Maier, J. Oxygen exchange kinetics on systematically doped ceria: a pulsed isotope exchange study. *J. Mater. Chem. A* **7**, 21854–21866 (2019).
50. Tsvetkov, N., Lu, Q., Sun, L., Crumlin, E. J. & Yildiz, B. Improved chemical and electrochemical stability of perovskite oxides with less reducible cations at the surface. *Nat. Mater.* **15**, 1010 (2016).
51. Feng, Z. a., El Gabaly, F., Ye, X., Shen, Z.-X. & Chueh, W. C. Fast vacancy-mediated oxygen ion incorporation across the ceria–gas electrochemical interface. *Nat. Commun.* **5**, 4374 (2014).
52. Mueller, D. N., Machala, M. L., Bluhm, H. & Chueh, W. C. Redox activity of surface oxygen anions in oxygen-deficient perovskite oxides during electrochemical reactions. *Nat. Commun.* **6**, 6097 (2015).
53. Frank Ogletree, D., Bluhm, H., Hebenstreit, E. D. & Salmeron, M. Photoelectron spectroscopy under ambient pressure and temperature conditions. *Nucl. Instruments Methods Phys. Res. Sect. A Accel. Spectrometers, Detect. Assoc. Equip.* **601**, 151–160 (2009).
54. Whaley, J. A. *et al.* Note: Fixture for characterizing electrochemical devices in-operando in traditional vacuum systems. *Rev. Sci. Instrum.* **81**, (2010).

Acknowledgments

This work was supported by the National Science Foundation under Award No. 1336835. MIT researcher was supported by grant DE SC0002633 funded by the U.S. Department of Energy, Office of Basic Science. The Advanced Light Source was supported by the Director, Office of Science, Office of Basic Energy Sciences, and the Division of Chemical Sciences, Geosciences, and Biosciences of the US Department of Energy at the Lawrence Berkeley National Laboratory under Contract No. DE-AC02-05CH11231. The authors thank Dr. Chia-Chin Chen from Stanford University and Dr. Qiyang Lu from Oak Ridge National Lab for critical reading of the manuscript and helpful discussion on XAS. The authors thank Qiaoyao Xu and Weikang Zhong from Tsinghua University for helpful discussion on data visualization.

Author contributions

D.C. designed the experiment. Z.G. derived the general microkinetic model for MIECs, and D.C. adapted the model for this study. D.C., Z.G., and D.Z. performed the experiments. S.N., L.T., E.C. and H.B. supported beamline experiments. D.C. analyzed the data. D.C., H.L.T., and W.C.C. wrote the manuscript. All authors revised the manuscript. W.C.C. supervised the project.

Competing interests

The authors declare no competing interests.

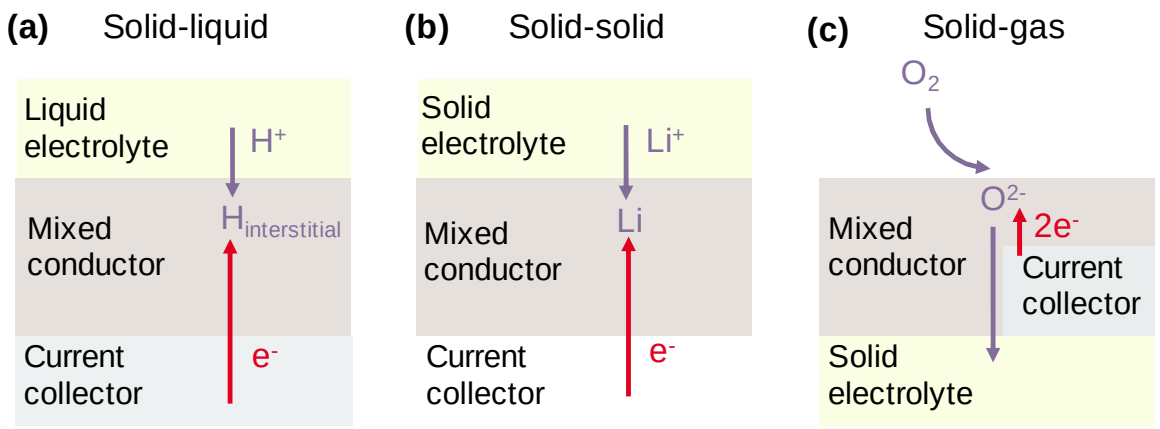

Figure 1 | Examples of mixed ion and electron transfer (MIET) reactions. (a) Proton intercalation in hydroxides occurring at the liquid–solid interface, **(b)** lithium intercalation in metal oxides occurring at the solid–solid interface, and **(c)** oxygen incorporation reaction occurring at the solid–gas interface.

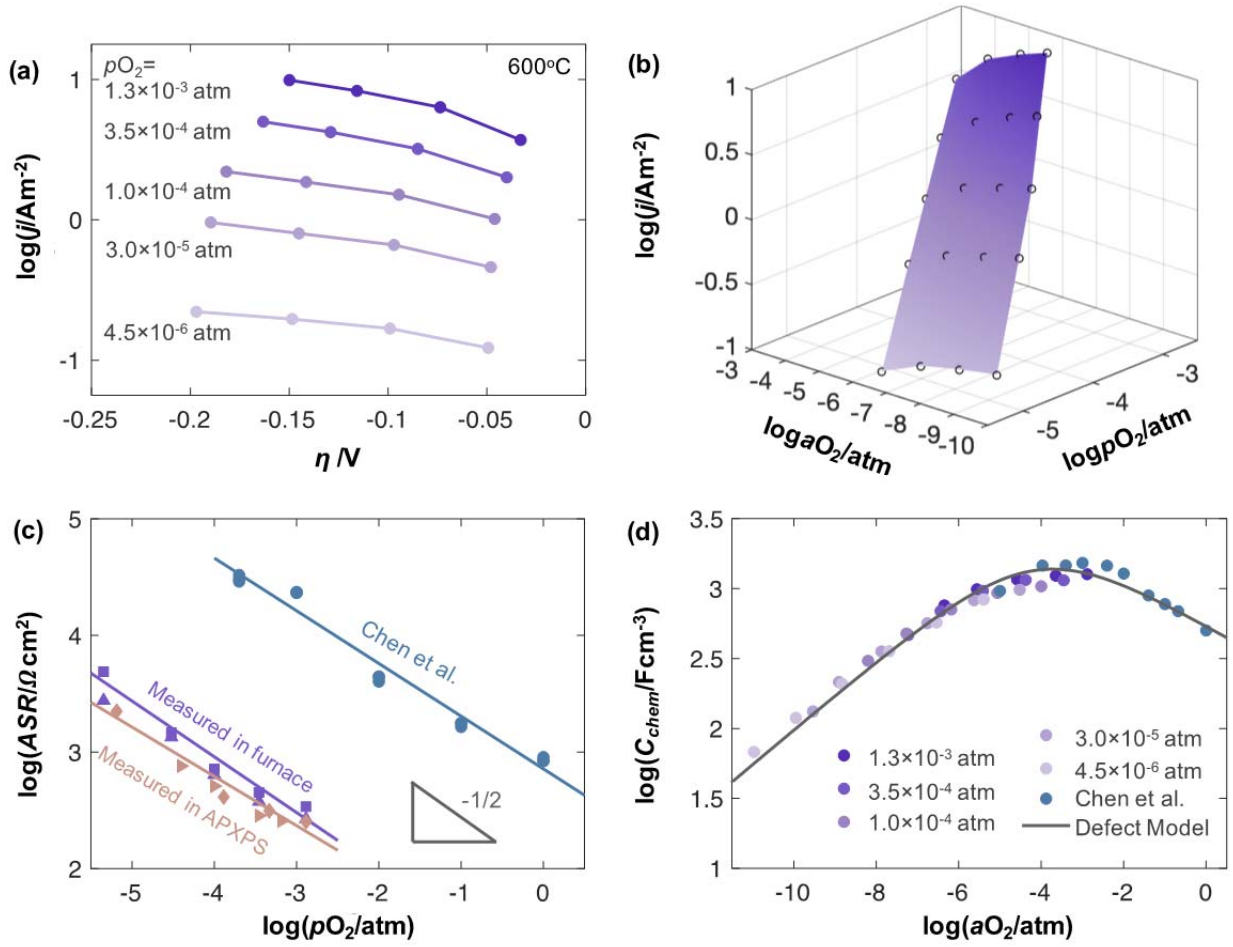

Figure 2 | Electrochemical measurement results. (a) Overpotential dependence of current density of PCO at 600 °C. The symbols indicate experimental data. The lines are used to guide the eye. The overpotential is Ohmic-corrected and validated by C_{chem} and peak shift in APXPS spectra. **(b)** Reconstruction of (a) vs. pO_2 and aO_2 using Eq. 8. The curved surface is 2D fitting of the experimental results. **(c)** pO_2 dependence of open-circuit area-specific resistance (ASR) (symbols) of PCO at 600 °C. The purple symbols indicate experimental data from this study, measured in a tube furnace. The peach symbols indicate experimental data from this study, measured in the APXPS chamber. The navy symbols indicate experimental data from literature, measured in a tube furnace, using quartz tube as the testing tube and Au paste as the current collector.[36] Solid lines represent linear fitting of the experimental data. **(d)** aO_2 dependence of

542 volume-specific chemical capacitance (C_{chem}) of PCO film at 600 °C. The symbols indicate
543 experimental data in this study compared with literature.[36] Solid line represents fit of bulk defect
544 model to experimental data.

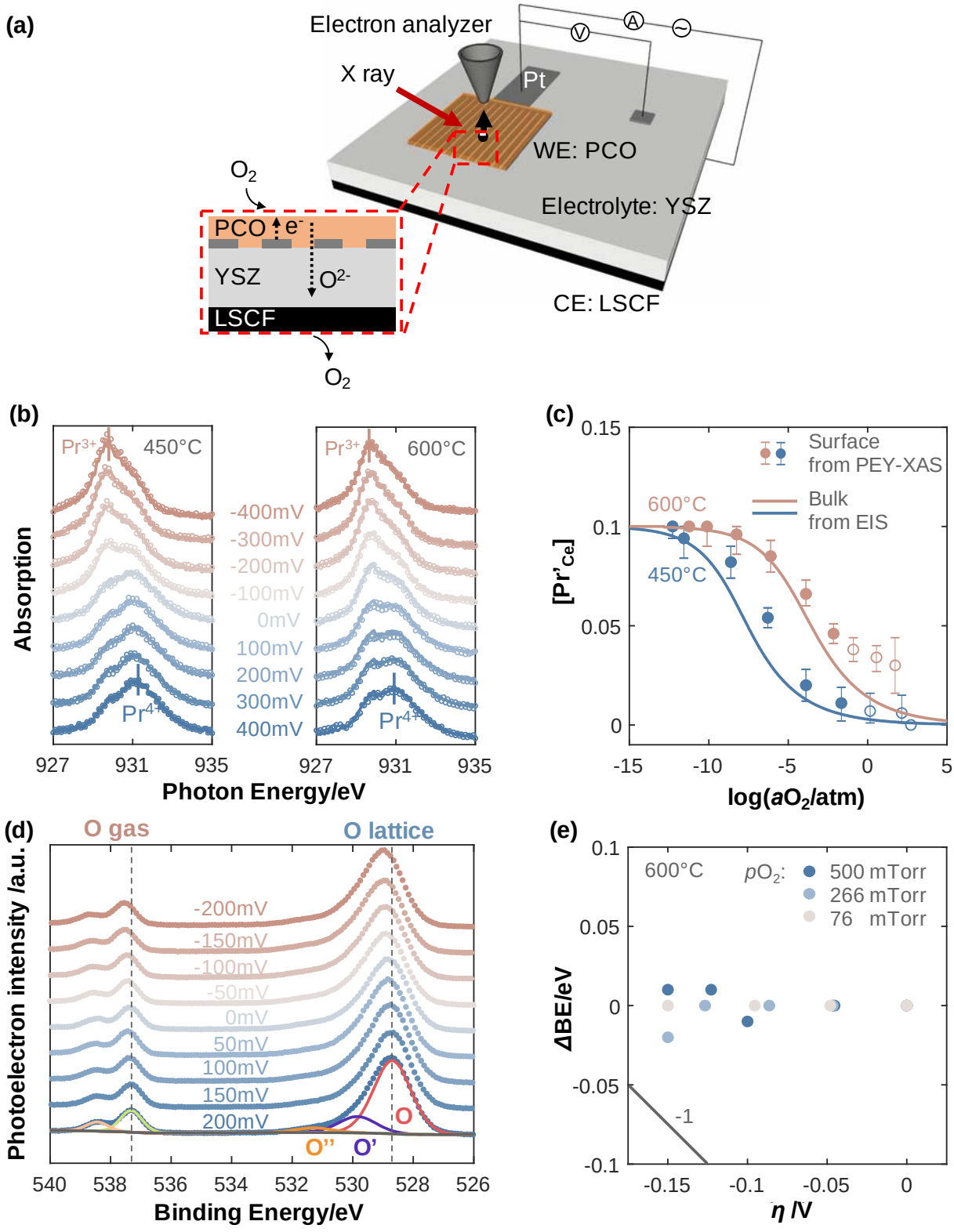

Figure 3 | Experimental setup and evolution of surface electron concentration and surface potential with overpotential. (a) A schematic depicting the experimental setup. The cell is

based on yttria-stabilized zirconia (YSZ) solid-oxide electrolyte, with dense PCO as the working electrode and $(La_{0.6}Sr_{0.4})(Co_{0.2}Fe_{0.8})O_3$ (LSCF) as the counter electrode. Patterned Pt is embedded in PCO thin film for efficient current collection. **(b)** Pr M_4 edge measured by ambient pressure X ray absorption spectra (APXAS) in partial electron yield detection mode at 450°C and 600 °C at pO_2=100mTorr, as a function of overpotential. The symbols are experimental data. The lines are linear combination fitting of spectra under the most oxidized (450 °C, +400mV) and reduced (600 °C, -400mV) conditions. **(c)** aO_2 dependence of the small polaron concentration (Pr^{3+} in PCO) on the surface measured by APXAS (symbols), and in the bulk calculated using chemical capacitance data (solid lines). The aO_2 of the filled symbols were validated by chemical capacitance. The aO_2 of the empty symbols could not be validated by chemical capacitance because their impedance spectra are highly distorted. Error bars are reported for an approximate 99% confidence of the linear combination. **(d)** Normalized O 1s APXPS spectra at various overpotential at 600 °C in $6.6x10^{-4}$atm (500 mTorr). The overpotential is validated by C_{chem}. For lattice oxygen peak, the main peak in red and shoulder peaks in purple and orange are due to lattice oxygen (O), oxygen bonded to the Si impurity (O') and surface O (O''), respectively. Spectra were taken at a photon energy of 690 eV corresponding to a probing depth of 0.6 nm. The binding energy (BE) is calibrated with the Au $4f_{7/2}$ peak of gold foil connected to the PCO electrode. **(e)** The shift of surface potential with overpotential at 600 °C. The values are plotted relative to open-circuit conditions.

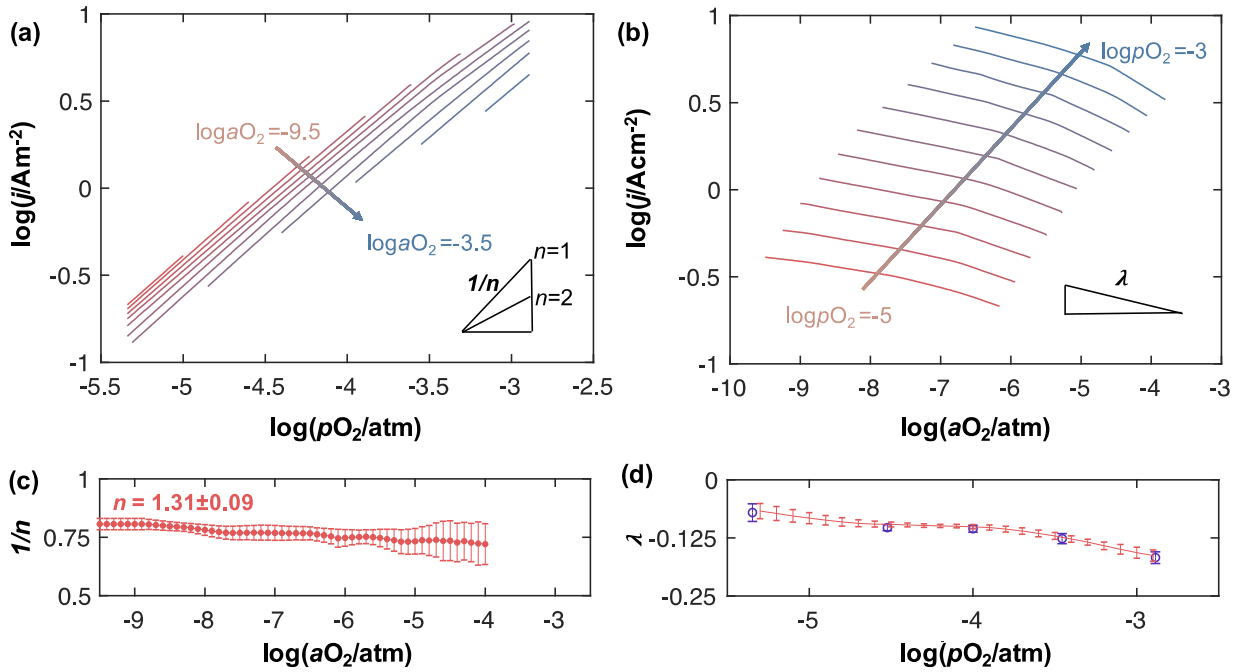

Figure 4 | Reaction orders for OIR. (a) pO_2 dependence of current density at several constant aO_2. **(b)** aO_2 dependence of current density at several constant pO_2. **(c)** The reaction orders $1/n$ and λ calculated from (a) and (b). The error bars are calculated from three electrodes.

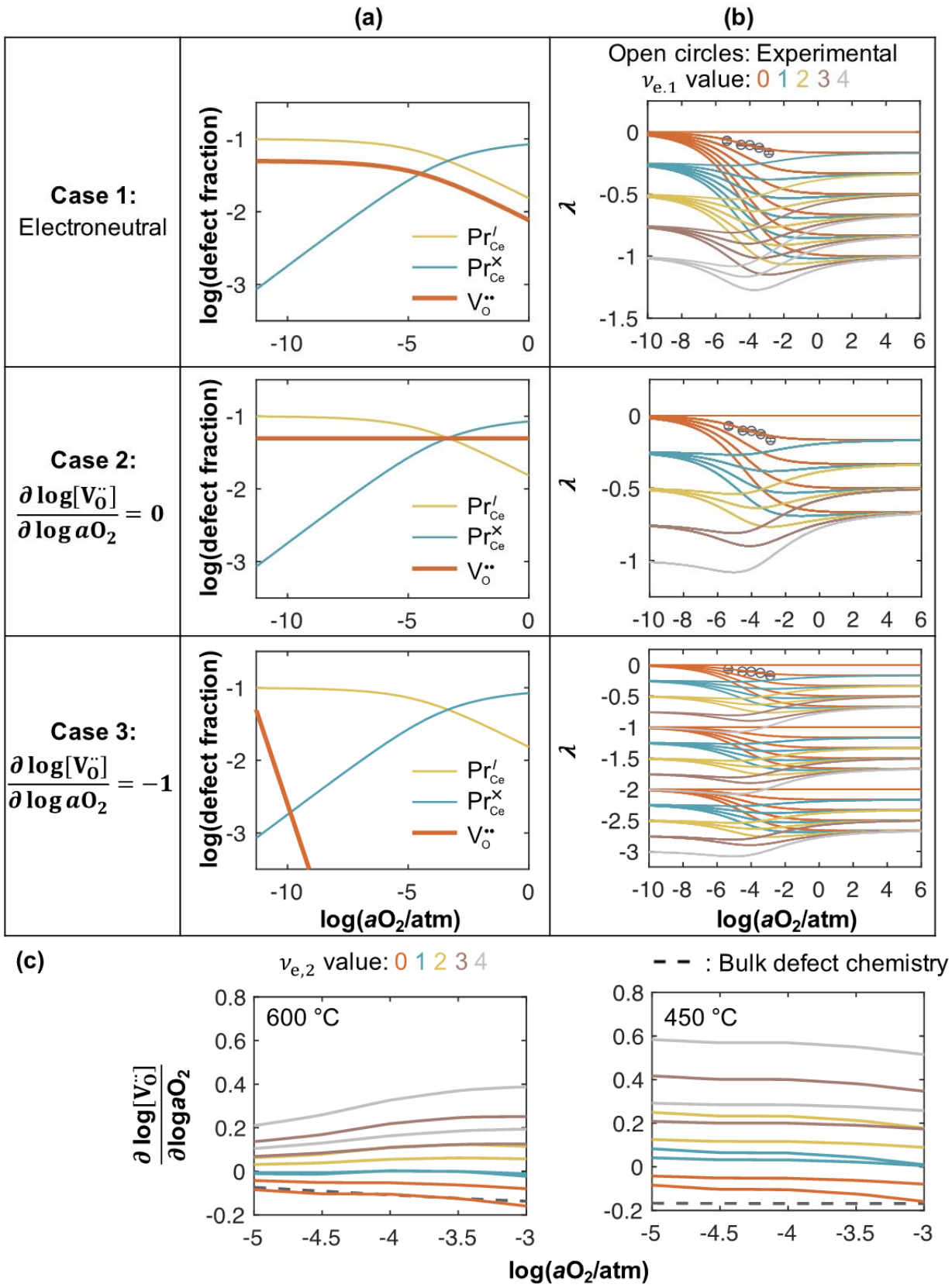
(a)
(b)
Case 1:
Electroneutral
Case 2:
$\frac{\partial \log[V_O^{\cdot\cdot}]}{\partial \log aO_2} = 0$
Case 3:
$\frac{\partial \log[V_O^{\cdot\cdot}]}{\partial \log aO_2} = -1$
log(defect fraction)
Pr'_{Ce}
$Pr^{\times}_{Ce}$
$V_O^{\cdot\cdot}$
Open circles: Experimental
$\nu_{e,1}$ value: 0 1 2 3 4
λ
log(aO_2/atm)
(c)
$\nu_{e,2}$ value: 0 1 2 3 4
– – : Bulk defect chemistry
600 °C
450 °C
$\frac{\partial \log[V_O^{\cdot\cdot}]}{\partial \log aO_2}$
log(aO_2/atm)

571

Figure 5 | Obtain reaction stoichiometric coefficients ($\nu_{V,i}$ and $\nu_{e,i}$) by analyzing $\boldsymbol{\lambda}$. (a) The dependence of simulated defect concentrations on aO_2 in PCO at 600 °C, with different $\frac{\partial \log[V_O^{\cdot\cdot}]}{\partial \log aO_2}$ as noted. **(b)** The simulated aO_2 dependence of $\boldsymbol{\lambda}$. The solid lines are calculated by Eq. 8, with the defect concentrations as shown in (a). Different lines are calculated with different $\nu_{e,1}$ values, as indicated by different colors. The symbols are experimental data. **(c)** The aO_2 dependence of $\frac{\partial \log[V_O^{\cdot\cdot}]}{\partial \log aO_2}$ at 600 °C and 450 °C. The solid lines are back-calculated from the experimental $\boldsymbol{\lambda}$ using Eq. 8. Different lines are calculated with different $\nu_{e,2}$ values, as indicated by different colors. The dashed line shows bulk experimental values.

	$\nu_{V,1}$	$\nu_{V,2}$	$\nu_{V,3}$	$\nu_{e,1}$	$\nu_{e,2}$	$\nu_{e,3}$	Initial State of RDS	Final State of RDS
A	0	0	2	0	0	4		
B	0	1	1	0	0	4	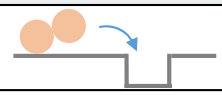	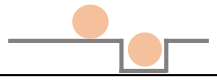
C	0	2	0	0	0	4		
D	1	0	1	0	0	4	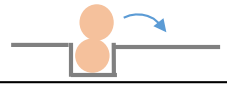	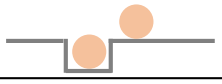
E	1	1	0	0	0	4	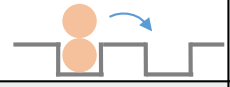	
F	2	0	0	0	0	4		

Figure 6 | Reaction mechanism. Combinations of stoichiometric coefficients that satisfy the condition $\nu_{e,1} = \nu_{e,2} = 0$ with their corresponding RDS and final state. The shaded combinations are unlikely. Here $\nu_{V,1}$, $\nu_{V,2}$ and $\nu_{V,3}$ are stoichiometric coefficients corresponding to the number of oxygen vacancies participating in the preceding, rate-determining, and following steps. Analogously, $\nu_{e,1}$, $\nu_{e,2}$, and $\nu_{e,3}$ are the stoichiometric coefficients of the electrons in these steps.

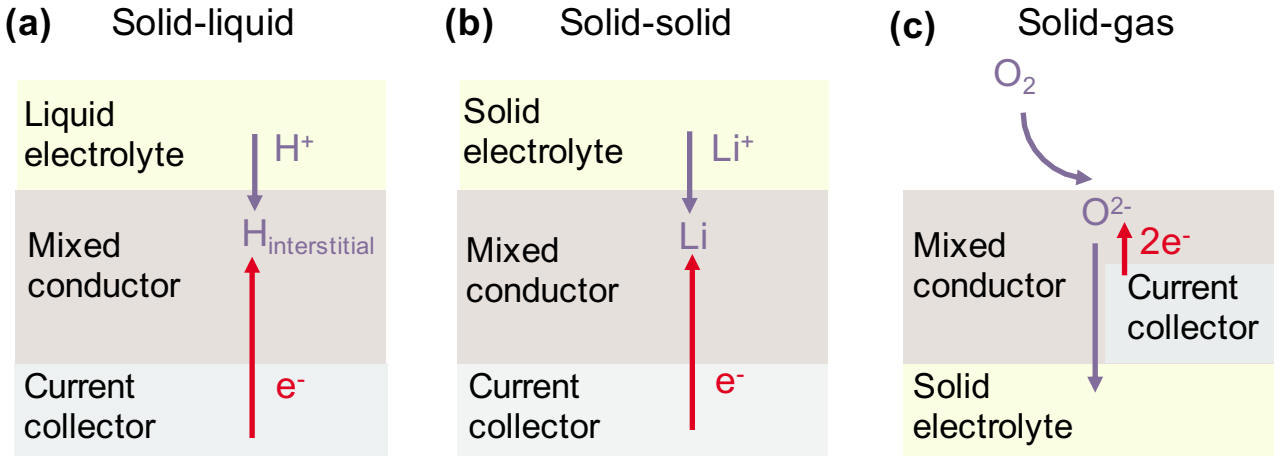
(a)
Solid-liquid
Liquid electrolyte
H+
Mixed conductor
H interstitial
Current collector
e-
(b)
Solid-solid
Solid electrolyte
Li+
Mixed conductor
Li
Current collector
e-
(c)
Solid-gas
O2
O2-
2e-
Mixed conductor
Current collector
Solid electrolyte

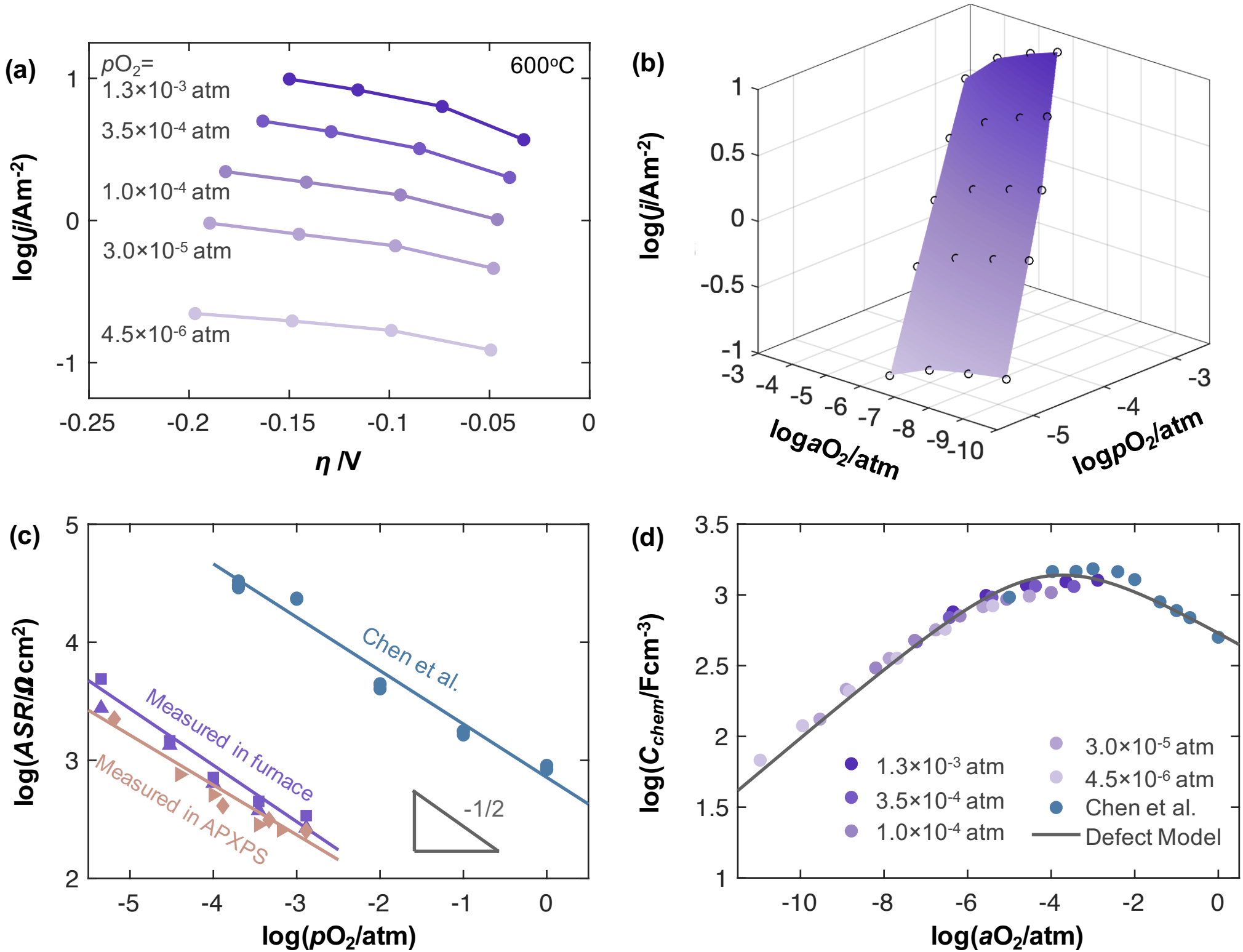
(a)
pO2=
600°C
1.3×10-3 atm
3.5×10-4 atm
1.0×10-4 atm
3.0×10-5 atm
4.5×10-6 atm
log(j/Am-2)
η /V
(b)
log(j/Am-2)
logaO2/atm
logpO2/atm
(c)
log(ASR/Ωcm2)
Chen et al.
Measured in furnace
Measured in APXPS
-1/2
log(pO2/atm)
(d)
log(Cchem/Fcm-3)
1.3×10-3 atm
3.5×10-4 atm
1.0×10-4 atm
3.0×10-5 atm
4.5×10-6 atm
Chen et al.
Defect Model
log(aO2/atm)

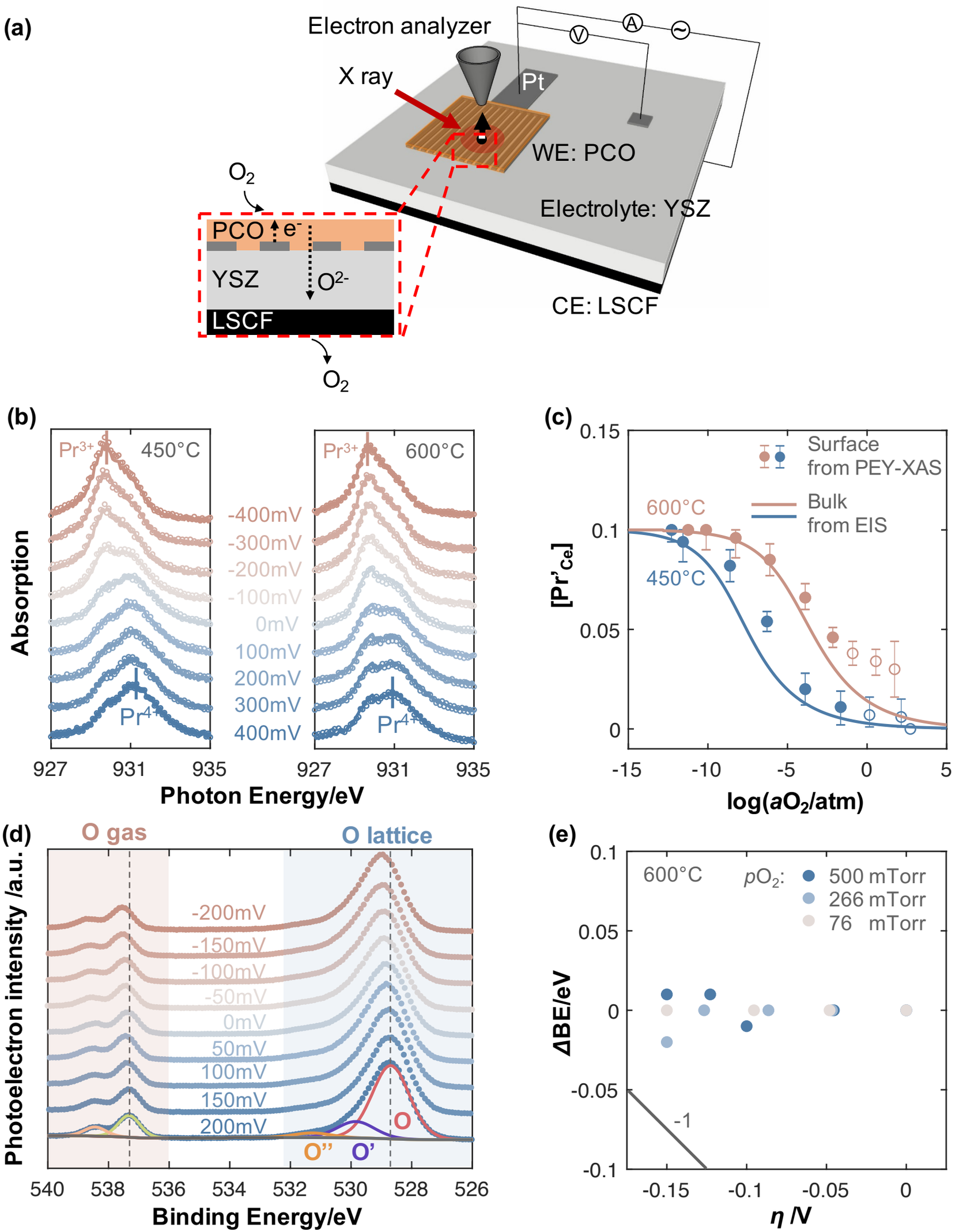
(a)
Electron analyzer
X ray
Pt
WE: PCO
Electrolyte: YSZ
CE: LSCF
O2
PCO
e-
YSZ
O2-
LSCF
O2
(b)
Pr3+
450°C
Pr3+
600°C
-400mV
-300mV
-200mV
-100mV
0mV
100mV
200mV
300mV
400mV
Pr4+
Pr4+
Absorption
927
931
935
927
931
935
Photon Energy/eV
(c)
0.15
0.1
0.05
0
Surface
from PEY-XAS
Bulk
from EIS
600°C
450°C
[Pr'Ce]
-15
-10
-5
0
5
log(aO2/atm)
(d)
O gas
O lattice
-200mV
-150mV
-100mV
-50mV
0mV
50mV
100mV
150mV
200mV
O
O''
O'
Photoelectron intensity /a.u.
540
538
536
534
532
530
528
526
Binding Energy/eV
(e)
0.1
0.05
0
-0.05
-0.1
600°C
pO2:
500 mTorr
266 mTorr
76 mTorr
-1
ΔBE/eV
-0.15
-0.1
-0.05
0
η /V

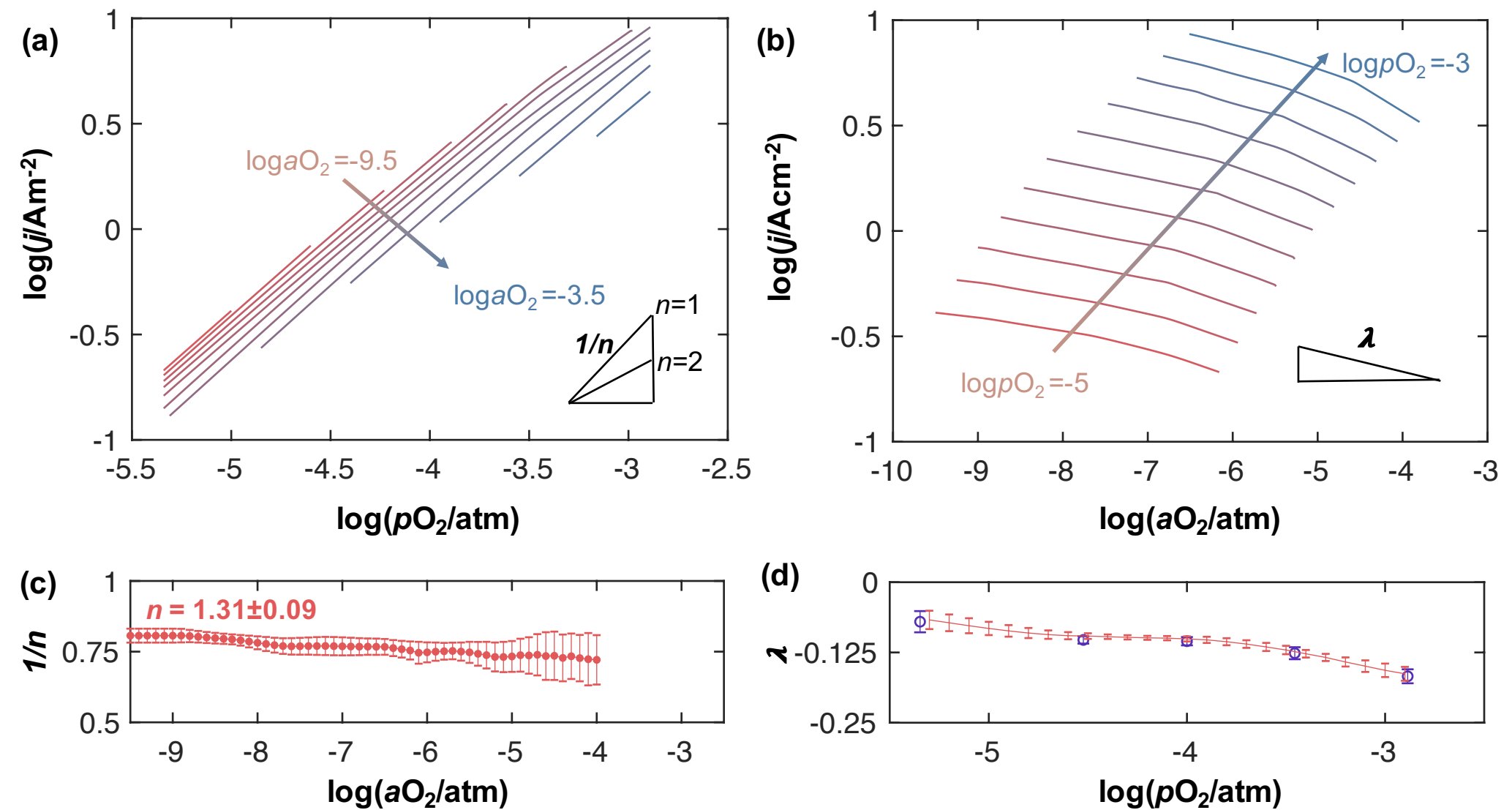
(a)
log(j/Am-2)
log(pO2/atm)
logaO2=-9.5
logaO2=-3.5
n=1
1/n
n=2
(b)
log(j/Acm-2)
log(aO2/atm)
logpO2=-3
logpO2=-5
λ
(c)
1/n
n = 1.31±0.09
log(aO2/atm)
(d)
λ
log(pO2/atm)

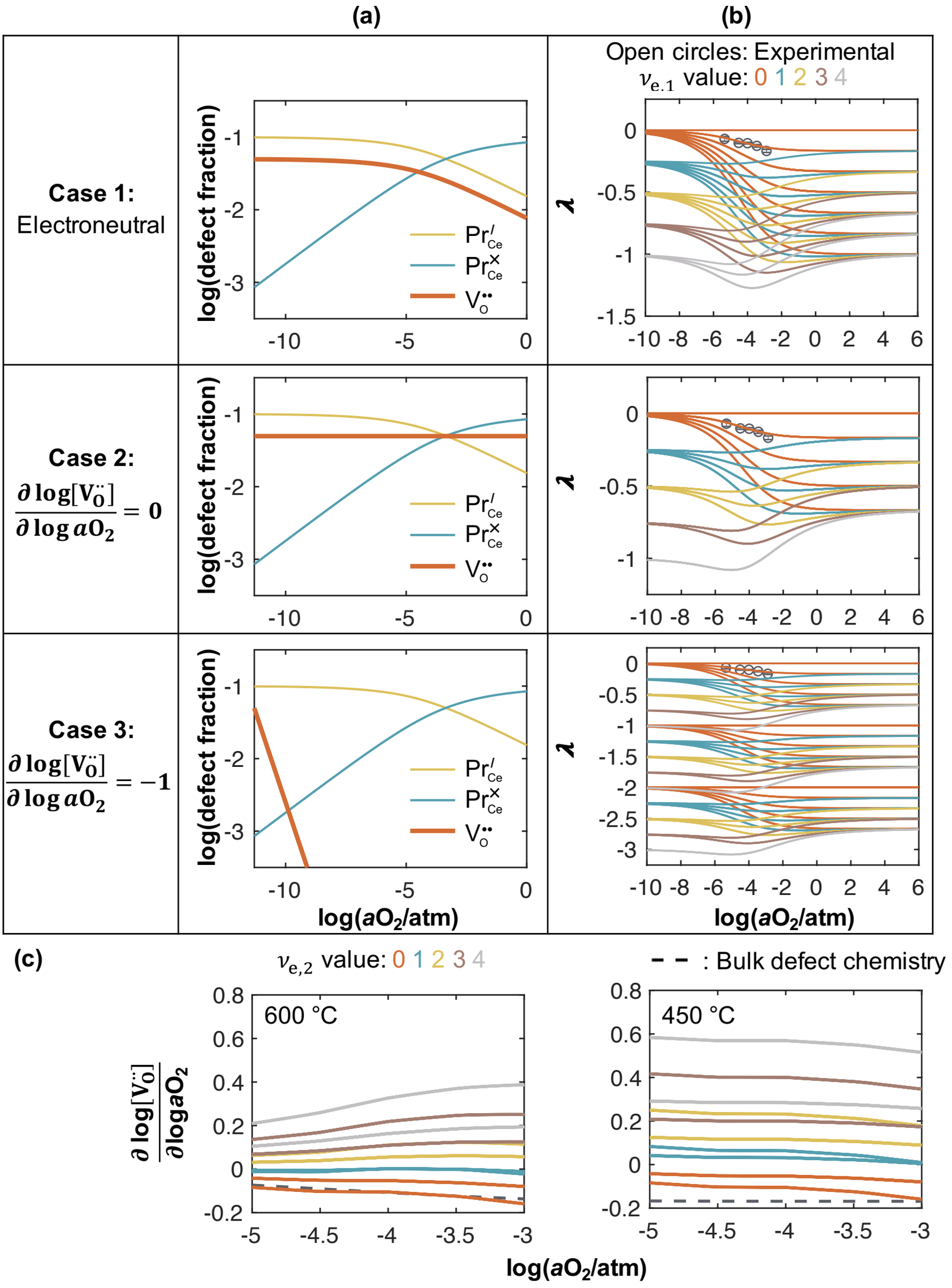
(a)
(b)
Case 1:
Electroneutral
Case 2:
$\frac{\partial \log[V_O^{\cdot\cdot}]}{\partial \log aO_2} = 0$
Case 3:
$\frac{\partial \log[V_O^{\cdot\cdot}]}{\partial \log aO_2} = -1$
log(defect fraction)
Pr'_{Ce}
$Pr^{\times}_{Ce}$
$V_O^{\cdot\cdot}$
Open circles: Experimental
$\nu_{e,1}$ value: 0 1 2 3 4
λ
log(aO_2/atm)
(c)
$\nu_{e,2}$ value: 0 1 2 3 4
– – : Bulk defect chemistry
600 °C
450 °C
$\frac{\partial \log[V_O^{\cdot\cdot}]}{\partial \log aO_2}$
log(aO_2/atm)

	$\nu_{V,1}$	$\nu_{V,2}$	$\nu_{V,3}$	$\nu_{e,1}$	$\nu_{e,2}$	$\nu_{e,3}$	Initial State of RDS	Final State of RDS
A	0	0	2	0	0	4		
B	0	1	1	0	0	4	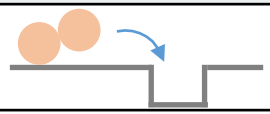	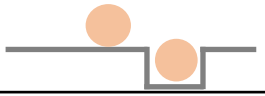
C	0	2	0	0	0	4	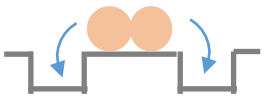	
D	1	0	1	0	0	4	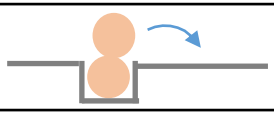	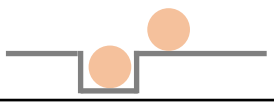
E	1	1	0	0	0	4	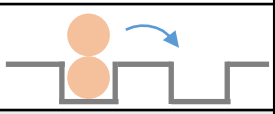	
F	2	0	0	0	0	4		

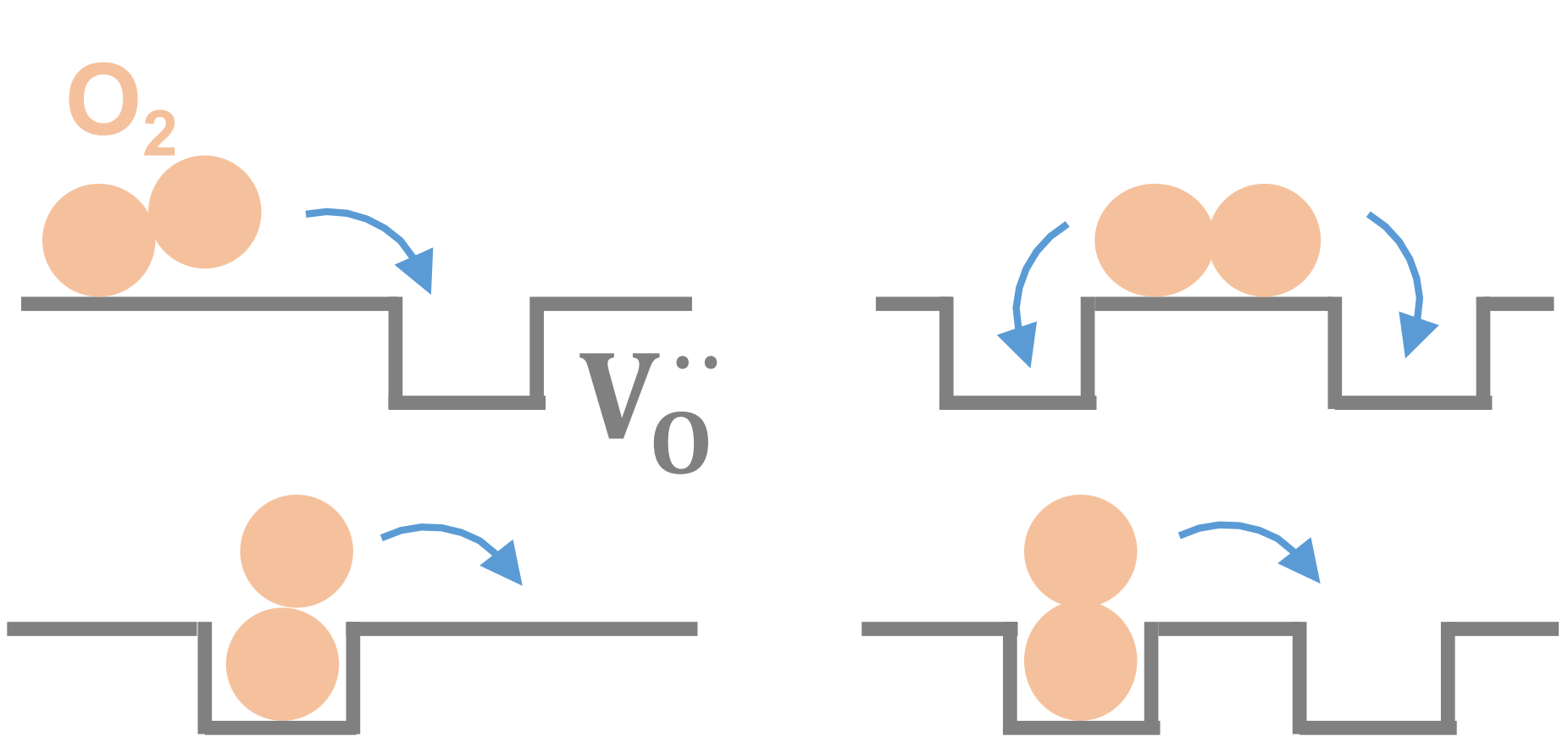
O2
V0..